Quantifying bone thickness, light transmission, and contrast interrelationships in transcranial photoacoustic imaging

Muyinatu A. Lediju Bell,[*a] Anastasia K. Ostrowski,[a,b] Ke Li,[c] Peter Kazanzides,[a] and Emad Boctor[a,d]

[a]Department of Computer Science, Johns Hopkins University, Baltimore, MD, USA
[b]Department of Biomedical Engineering, University of Michigan, Ann Arbor, MI, USA
[c]Department of Biomedical Engineering, Johns Hopkins University, Baltimore, MD, USA
[d]Department of Radiology, Johns Hopkins University, Baltimore, MD, USA

ABSTRACT

We previously introduced photoacoustic imaging to detect blood vessels surrounded by bone and thereby eliminate the deadly risk of carotid artery injury during endonasal, transsphenoidal surgeries. Light would be transmitted through an optical fiber attached to the surgical drill, while a transcranial probe placed on the temporal region of the skull receives photoacoustic signals. This work quantifies changes in photoacoustic image contrast as the sphenoid bone is drilled. Frontal bone from a human adult cadaver skull was cut into seven 3 cm x 3 cm chips and sanded to thicknesses ranging 1-4 mm. For 700-940 nm wavelengths, the average optical transmission through these specimens increased from 19% to 44% as bone thickness decreased, with measurements agreeing with Monte Carlo simulations within 5%. These skull specimens were individually placed in the optical pathway of a 3.5 mm diameter, cylindrical, vessel-mimicking photoacoustic target, as the laser wavelength was varied between 700-940 nm. The mean optical insertion loss and photoacoustic image contrast loss due to the bone specimens were 56-80% and 46-79%, respectively, with the majority of change observed when the bone was ≤ 2 mm thick. The decrease in contrast is directly proportional to insertion loss over this thickness range by factors of 0.8-1.1 when multiple wavelengths are considered. Results suggest that this proportional relationship may be used to determine the amount of bone that remains to be drilled when the thickness is 2 mm or less.

Keywords: transcranial imaging, optoacoustic imaging, pituitary tumors, image-guided surgery, skull base surgery, tumor resection, optical transmission, bone

1. INTRODUCTION

Endonasal, transsphenoidal surgery is the most common approach to remove pituitary tumors located at the base of the brain. Although the surgery is generally safe, one of the most significant complications is caused by the location of the carotid arteries within 1-7 mm of the pituitary gland.[1,2] Accidental injury to the carotid arteries is a serious surgical setback that causes extreme blood loss, thrombosis, delayed neurological deficits, strokes, and possibly death, with 14% morbidity and 24-40% mortality rates.[3,4] A real-time Doppler ultrasound probe was developed to assist surgeons with detecting carotid arteries,[5] but it failed in at least one case due to misinterpretation of images and Doppler signals, resulting in misjudgment of the carotid artery location.[2] Thus, there remains a salient need for real-time imaging methods that eliminate carotid artery injury during surgery.

We previously proposed photoacoustic imaging to provide real-time, intraoperative visualization of blood vessels located behind bone.[6] Light would be transmitted through an optical fiber attached to the surgical drill, while a transcranial ultrasound probe placed on the temporal region of the skull receives photoacoustic signals. Other types of transcranial photoacoustic prototypes have been proposed with the light and probe external to the skull. These prototypes demonstrated feasibility with phantoms, human adult skull, monkey skulls, and monkey brains.[7–9] Wang et al.[10] additionally reported 60-70% light transmission through a 0.6-0.9 mm thick infant skull, and this transmission was sufficient to visualize a 50 μm target comprised of canine blood located approximately 2 cm below the bone surface. These studies provide evidence that our proposed system has potential to guide

---

*E-mail:muyinatu.ledijubell@jhu.edu

transphenoidal surgeries, as the sphenoid bone is 0.4-8.8 mm thick,[11, 12] located up to 1.37 cm away from the internal carotid arteries,[13] which have diameters of 3.7-8.0 mm.[14]

The penetration of light through the sphenoid bone and hence the quality of resulting photoacoustic images is expected to improve as the sphenoid bone is removed, given the proportional relationships between optical transmission through bone, laser fluence incident on underlying vessels, and photoacoustic signal amplitude. However, to the authors' knowledge, no experimental studies directly measure these relationships. The purpose of this work is to quantify the expected improvements in signal contrast and optical penetration as bone thickness decreases due to the drilling process, with additional applicability to identifying candidates for more general transcranial photoacoustic imaging based on skull thickness.

2. METHODS

2.1 Photoacoustic Experiments

A plastisol phantom was fabricated with no optical or acoustic scatterers to isolate effects due to the presence of bone. A 3 mm diameter hole was drilled into the phantom and a black, cylindrical rubber target with a diameter of 3.5 mm was inserted into the hole. This target was chosen for its similar diameter to the internal carotid artery[14] and to achieve an optical absorption at least an order of magnitude greater than bone (similar to blood).[15–17] The target is not expected to significantly vary with wavelength in order to separate the effects of bone penetration from blood absorption as a function of wavelength.

A human frontal skull bone was cut into seven 3 cm x 3 cm specimens and sanded to thicknesses ranging 1.0-4.0 mm (measured with calipers), as shown in Fig. 1(a). Note that although bone thickness was controlled, there were subtle variations among the specimens (e.g. embedded vessels, bone color) that could cause variations in the optical properties. A slit was cut approximately 1 cm from vessel and the skull specimens were individually placed in the slit to obstruct the optical path, as shown in Fig. 1(b). Light was transmitted from the 5-mm diameter optical fiber bundle coupled to a combined Nd:YAG laser and optical parametric oscillator (OPO) system (Phocus InLine, Opotek, Carlsbad, CA) which tuned the wavelength from 700 nm to 940 nm, in 20 nm increments. An Ultrasonix L14-5W/60 linear transducer with a bandwidth of 5-14 MHz was placed with the long axis of the vessel perpendicular to the axial dimension of the probe. The transducer was connected to a SonixTouch ultrasound scanner, and a SonixDAQ data acquisition unit was triggered by the flashlamp output signal of the laser to access raw, pre-beamformed radiofrequency photoacoustic data.

Photoacoustic images were reconstructed with a delay-and-sum beamformer and the resulting contrast was measured as follows:

$$\text{Contrast} \; = \; 20\log_{10}\left(\frac{S_i}{S_o}\right) \tag{1}$$

where S_i and S_o are the means of the image data within regions of interest (ROIs) located inside and outside of the target, respectively, and σ_o is the standard deviation of the data within the ROI located outside of the target. ROIs were defined by searching for the maximum signal within the expected signal location, surrounding this signal with a rectangle, and automatically creating a same-sized noise ROI at the same depth to the right of the signal ROI. Contrast measurements were averaged over five independent acquisitions.

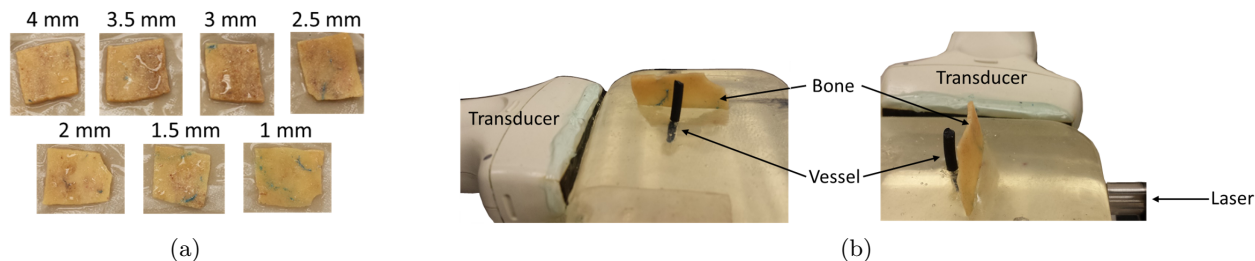

(a)   (b)

Figure 1. Photographs of (a) skull bone sanded to the thicknesses indicated above each image and (b) the experimental setup.

The contrast loss due to the placement of bone, C_{loss}, was measured as follows:

$$C_{loss} = \left(1 - \frac{C_b}{C_0}\right) \cdot 100\% \tag{2}$$

where C_0 is the contrast when no bone was placed and C_b is the contrast when one of the bone specimens was present. All image processing and data analyses were performed with MATLAB software (The MathWorks, Natick, MA).

2.2 Optical Transmission Measurements

The average energy per pulse was recorded with and without the bone inserted between the fiber and energy meter (NOVA, Ophir, Jerusalem, Israel) as the wavelength of laser was tuned from 700 nm to 940 nm, in increments of 20 nm. A 5 mm diameter fiber bundle delivered the light with an average pulse energy that varied between 6.3 mJ and 14.5 mJ with each wavelength. Transmission was calculated as the ratio between the energy measurements before insertion of the bone to that measured after bone insertion. This ratio was multiplied by 100 to report optical transmission as a percentage and converted to insertion loss measurements through the expression:

$$\text{Insertion Loss} = (1 - \text{Transmission Ratio}) \cdot 100\% \tag{3}$$

A one-layer tissue model with the average wavelength-dependent optical properties for skull bone,[18] as listed in Table 1, was used to estimate optical transmission through bone with a Monte Carlo simulation package.[19] The bone's thickness was varied between 0.5-4 mm in increments of 0.5 mm (which is within the range of sphenoid bone thickness[20]), the wavelength was varied between 700-940 nm, and the refractive index was held constant at 1.56.[16] The top and bottom ambient media were modeled as air with a refractive index of 1. The related optical insertion loss was calculated using Eq. 3. The parameters in Table 1 were additionally adjusted within the error of reported measurements[18] to find the best fit with our experimental data.

Table 1. Simulation parameters for absorption, μ_a (cm^{-1}), scattering, μ_s (cm^{-1}), and anisotropy factor (g)

| | Wavelength (nm) | | | | | | | | | | | | |
	700	720	740	760	780	800	820	840	860	880	900	920	940
μ_a	0.24	0.23	0.24	0.25	0.245	0.245	0.25	0.26	0.27	0.29	0.33	0.38	0.43
μ_s	333	326	320	313	306	300	293	286	280	273	266	260	253
g	0.932	0.935	0.936	0.937	0.938	0.938	0.938	0.939	0.939	0.940	0.941	0.943	0.944

3. RESULTS

Fig. 2 shows sample photoacoustic images of the target in Fig. 1(b), taken with 800 nm wavelength (13.1 mJ per pulse) in the presence of the bone thicknesses indicated above each image and when no bone was present (0 mm), representing the changes in vessel contrast that would be observed as the sphenoid bone is drilled. Only
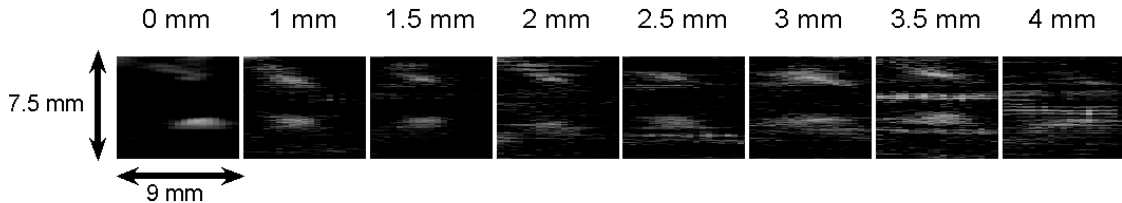

Figure 2. Photoacoustic images of the vessel-mimicking target acquired as the bone thickness indicated above each image obstructed the optical path. Each image is shown with 15 dB dynamic range and measures 7.5 mm x 9 mm (axial x lateral probe dimensions, respectively).

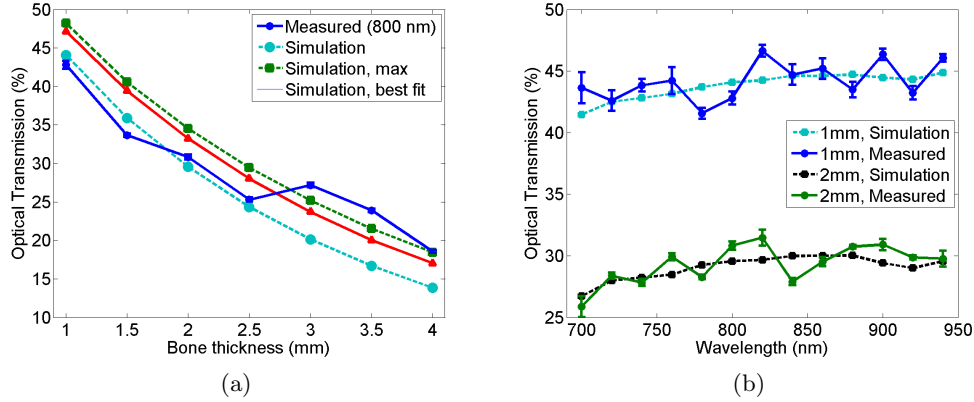(a)   (b)

Figure 3. Optical transmission ratios due to (a) varying bone thicknesses (at 800 nm laser wavelength) and (b) varying laser wavelengths (at 1 mm and 2 mm bone thicknesses), as measured with Monte Carlo simulations and experimental results. The optical parameters reported in Table 1 were additionally adjusted in (a) to obtain the best fit with experimental data as a function of thickness and the maximum optical transmission. Error bars indicate ± one standard deviation of three independent measurements for each wavelength and thickness, respectively.

the proximal and distal boundaries of the 3.5 mm diameter vessel are visible in these images. In addition, the signal appears less diffuse as bone thickness decreases.

Optical transmission measurements are shown as a function of bone thickness in Fig. 3(a) for both simulation and experimental measurements. In addition to the values reported in Table 1, the optical parameters were adjusted to obtain a "best fit" for all thicknesses ($\mu_s = 280\ cm^{-1}, g = 0.948$) as well as an "upper limit" (i.e. max in Fig. 3(a)) based on the error reported in previous measurements ($\mu_s = 270\ cm^{-1}, g = 0.948$).[18] With these adjustments, the simulation and experimental measurements differ by up to 5%. Note the measured transmission decreases up to 30% with increased thickness, a primary factor causing the poor image contrast observed with increased bone thickness in Fig 2.

The simulation results in Fig. 3(b) show optical transmission measurements as a function of laser wavelength for experimental measurements and simulation results based on the parameters reported in Table 1. Contrary to variations as a function of bone thickness, the optical transmission increases by less than 4% as the wavelength is varied, indicating that the change in bone thickness would have a greater effect on image contrast than the change caused by different laser wavelengths, particularly within the 700-940 nm range. For all wavelengths investigated, the mean optical transmission through the specimens increased from 19% to 44% as bone thickness
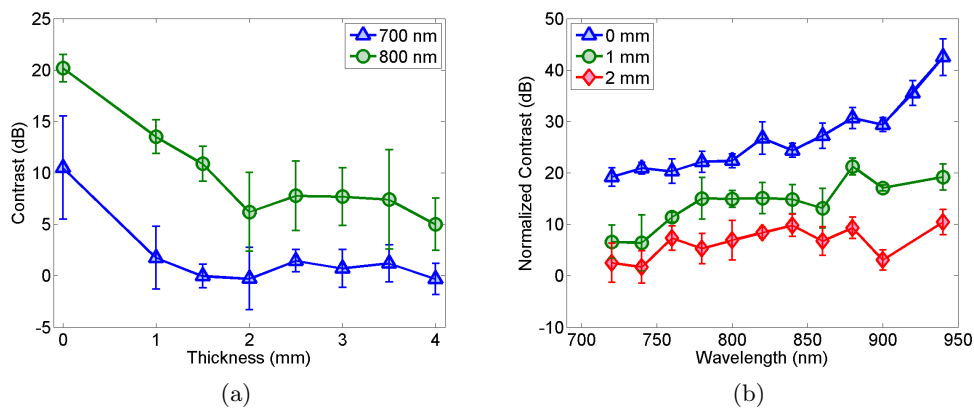

(a)   (b)

Figure 4. Contrast of the photoacoustic signal as a function of (a) bone thickness (for 700 and 800 nm wavelengths) and (b) laser wavelength (for 0, 1, and 2 mm bone thicknesses). Error bars represent ± one standard deviation of five independent measurements.

decreased from 4 mm to 1 mm.

Photoacoustic signal contrast is quantified as a function of bone thickness in Fig. 4(a) for laser wavelengths of 700 and 800 nm. Each data point shows the mean ± one standard deviation of five independent acquisitions. A majority of the changes in contrast occur for bone thicknesses ≤ 2 mm, which corresponds to measured transmission ratios ≥ 30%. Poor target visibility (e.g. contrast) was observed at wavelengths of 700 nm (Fig. 4(a)) and 920 nm (not shown), thus the data from these measurements were not included in subsequent analyses.

Contrast is shown as a function of wavelength in Fig. 4(b) for bone thicknesses of 0 mm (i.e. no bone), 1 mm, and 2 mm. The photoacoustic signal contrast was normalized for changes in laser energy as a function of wavelength, thus the contrast results for no bone depict the optical absorption spectra differences of the rubber target. When bone is present, contrast is increased by up to 20 dB as wavelength increases, which may be due to the increased absorption of the target or the increased optical penetration through bone (Fig. 3(b)).

The measured contrast loss as a function of bone thickness is shown in Fig. 5(a). The gray lines show individual means for each wavelength and black lines shown mean results for all wavelengths ± one standard deviation. Note that the combination of all wavelengths (i.e. the black line) reduces the variations in the measurements for each wavelength (i.e. the gray lines). With this combination of spectroscopic information, it is clear that contrast loss increases with thickness and appears saturated when the thickness is ≥ 2mm.

Fig. 5(b) directly relates contrast loss to insertion loss. For 56%, 66% and 70% mean optical insertion loss (i.e. 1, 1.5, and 2 mm bone thickness, respectively) the mean contrast loss is 46%, 64%, and 75%, respectively. The error bars show standard deviation and span ±10-13% and ±1-2% for the contrast loss and insertion loss measurements, respectively. A large component of this variation (e.g. up to 4% or 20 dB, respectively) is caused by the combination of all wavelengths. Nonetheless, this combination reduces variations in the measurements, revealing that changes in optical transmission are proportional to changes in image contrast, with scaling factors that range from 0.8 to 1.1, particularly when the bone thickness is ≤ 2mm.
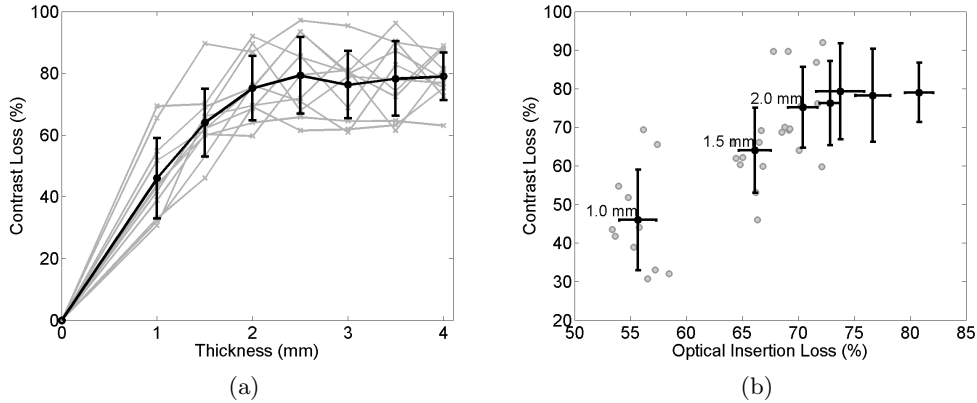

Figure 5. (a) Loss in contrast relative to the signal with no bone with gray lines showing individual means for each wavelength and black lines showing mean results for all wavelengths ± one standard deviation. (b) Mean contrast loss vs. mean optical insertion loss over 720-940 nm wavelengths with gray points showing measurements for each wavelength for 1, 1.5, and 2 mm bone thicknesses, black points showing the mean values for all wavelengths and all thicknesses (1, 1.5 and 2.0 mm thicknesses are noted next to the corresponding points). The error bars represent ± one standard deviation.

4. DISCUSSION

The expected relationships between optical transmission, bone thickness, and photoacoustic image contrast were confirmed, particularly for bone thicknesses of 2 mm or less. When the measured insertion loss was greater than 70% (i.e. less than 30% optical transmission, which corresponds with the 2.0 mm bone thickness), changes in contrast were subtle to nonexistent, likely because of anatomical variability, insufficient fluence to generate a photoacoustic signal, or low-amplitude signals that are difficult to detect with delay-and-sum beamforming. The latter challenge may be overcome with coherence-based beamforming,[6] which might be the preferred method for

vessel visualization when more than 2 mm of bone remains to be drilled. Otherwise, with an amplitude-based beamformer like delay-and-sum, the contrast of photoacoustic signals increases with decreasing bone thickness.

Over the 720-940 nm wavelength range, Wang et al[10] measured 60-70% optical transmission through an infant skull thickness of 0.6-0.9 mm. This is consistent with extrapolation of the results in Fig. 3(a). The work herein therefore extends previous measurements to a larger range of bone thicknesses. For the same wavelength range, the mean optical transmission through human adult skulls of thickness 1-4 mm is expected to increase from 14 to 49% as thickness decreases, with up to 5% deviation from expected values. This information may be used to identify successful candidates for transcranial imaging based solely on skull thickness.

Acoustic scattering and the presence of temporal bone between the transducer and phantom would reduce the final optical transmission measurements. Nonetheless, the presented experiments were designed to minimize the acoustic effects of transcranial photoacoustic imaging, which has been studied previously for human adult skulls with reports of approximately 0-40 dB acoustic insertion loss.[10, 21] In addition, the contrast loss relative to an initial measurement from the same acoustic environment, as illustrated in Fig. 5(a), is not expected to be affected by the presence of temporal bone.

A key finding from this work is the quantifiable scaling factor between contrast loss and optical insertion loss measurements for bone thicknesses of 2 mm or less when multiple wavelengths are considered. Otherwise, if contrast is relatively constant as bone is drilled, surgeons may assume that more than 2 mm of bone remains. The expected mean contrast change in photoacoustic signals due to drilling can potentially be predicted using the proposed spectroscopic approach if the optical transmission through bone and an initial bone thickness (determined from preoperative CT or MR images) are known. The patient-specific optical transmission could be provided by analyzing the initial specimens of sphenoid bone removed during an operation. If this type of analysis is unavailable (e.g. if the initial thickness of the sphenoid bone is 2 mm or less), Monte Carlo simulations may be utilized with an approximate 5% expected deviation between simulated and measured optical transmission, based on the results presented in Fig. 3(a). A contrast loss prediction that relies on either method may then be correlated with actual intraoperative contrast loss measurements to determine the amount of bone that remains to be drilled, which will be the focus of future work.

5. CONCLUSION

We quantified the proportional relationships between photoacoustic image contrast, bone thickness (≤ 2mm), and optical penetration with a spectroscopic approach that combines measurements from multiple wavelengths (720-940 nm). The scaling factor between contrast loss and insertion loss is 0.8-1.1 for bone thicknesses ≤ 2mm and is relatively constant for greater thicknesses due to minimal changes in image contrast. Results additionally demonstrate that the optical penetration through human adult skull bone of thickness 1 mm to 4 mm is 50% to 15%, respectively, and contrast is relatively constant for optical transmission greater than 30% (i.e. 70% insertion loss). This work lays the foundation for determining the amount of bone that remains to be drilled by monitoring image contrast during endonasal transsphenoidal surgeries.

REFERENCES

[1] G. R. Isolan, P. H. P. de Aguiar, E. R. Laws, A. C. P. Strapasson, and O. Piltcher. The implications of microsurgical anatomy for surgical approaches to the sellar region. *Pituitary*, 12(4):360–367, 2009.

[2] J. R. Dusick, F. Esposito, D. Malkasian, and D. F. Kelly. Avoidance of carotid artery injuries in transsphenoidal surgery with the doppler probe and micro-hook blades. *Neurosurgery*, 60(4):322–329, 2007.

[3] M. Perry, W. Snyder, and E. Thal. Carotid artery injuries caused by blunt trauma. *Annals of Surgery*, 192(1):74, 1980.

[4] J. Raymond, J. Hardy, R. Czepko, and D. Roy. Arterial injuries in transsphenoidal surgery for pituitary adenoma; the role of angiography and endovascular treatment. *American Journal of Neuroradiology*, 18(4):655–665, 1997.

[5] T. Yamasaki, K. Moritake, J. Hatta, and H. Nagai. Intraoperative monitoring with pulse doppler ultrasonography in transsphenoidal surgery: technique application. *Neurosurgery*, 38(1):95–98, 1996.

[6] M. A. Lediju Bell, A. K. Ostrowski, P. Kazanzides, and E. Boctor. Feasibility of transcranial photoacoustic imaging for interventional guidance of endonasal surgeries. In *SPIE BiOS*, pages 894307–894307. International Society for Optics and Photonics, 2014.

[7] L. Nie, X. Cai, K. Maslov, A. Garcia-Uribe, M. A. Anastasio, and L. V. Wang. Photoacoustic tomography through a whole adult human skull with a photon recycler. *Journal of Biomedical Optics*, 17(11):110506, 2012.

[8] C. Huang, L. Nie, R. W. Schoonover, Z. Guo, C. O. Schirra, M. A. Anastasio, and L. V. Wang. Aberration correction for transcranial photoacoustic tomography of primates employing adjunct image data. *Journal of Biomedical Optics*, 17(6):0660161–0660168, 2012.

[9] X. Yang and L. V. Wang. Monkey brain cortex imaging by photoacoustic tomography. *Journal of Biomedical Optics*, 13(4):044009–044009, 2008.

[10] X. Wang, D. L. Chamberland, and G. Xi. Noninvasive reflection mode photoacoustic imaging through infant skull toward imaging of neonatal brains. *Journal of Neuroscience Methods*, 168(2):412–421, 2008.

[11] N. Lazaridis, K. Natsis, J. Koebke, and C. Themelis. Nasal, sellar, and sphenoid sinus measurements in relation to pituitary surgery. *Clinical Anatomy*, 23(6):629–636, 2010.

[12] Hosemann, W. and Gross, R. and Göde, U. and Kühnel, T. and Röckelein, G. The anterior sphenoid wall: relative anatomy for sphenoidotomy. *American Journal of Rhinology*, 9(3):137–144, 1995.

[13] J. R. Tatreau, M. R. Patel, R. N. Shah, K. A. McKinney, S. A. Wheless, B. A. Senior, M. G. Ewend, A. V. Germanwala, C. S. Ebert, and A. M. Zanation. Anatomical considerations for endoscopic endonasal skull base surgery in pediatric patients. *The Laryngoscope*, 120(9):1730–1737, 2010.

[14] H. Takegoshi and S. Kikuchi. An anatomic study of the horizontal petrous internal carotid artery: sex and age differences. *Auris Nasus Larynx*, 34(3):297–301, 2007.

[15] S. Prahl. *Tabulated molar extinction coefficient for hemoglobin in water*. Oregon Medical Laser Center, 1998.

[16] E. A. Genina, A. N. Bashkatov, and V. V. Tuchin. *Optical clearing of the cranial bone*. 2008.

[17] V. der Zee, E. Pieter, Matthias, and D. T. Delpy. Optical properties of brain tissue. *Proc. SPIE 1888, Photon Migration and Imaging in Random Media and Tissues*, 454, 1993.

[18] M. Firbank, M. Hiraoka, M. Essenpreis, and D. T. Delpy. Measurements of the optical properties of the skull in the wavelength range 650-950 nm. *Physics in Medicine and Biology*, 38(4):503–510, 1992.

[19] L. Wang, S. L. Jacques, and L. Zheng. MCML–Monte Carlo modeling of light transport in multi-layered tissues. *Computer Methods and Programs in Biomedicine*, 47(2):131–146, 1995.

[20] W. H. Renn and A. L. Rhoton Jr. Microsurgical anatomy of the sellar region. *Journal of Neurosurgery*, 43(3):288–298, 1975.

[21] F. J. Fry and J. E. Barger. Acoustical properties of the human skull. *The Journal of the Acoustical Society of America*, 63(5):1576–1590, 1977.